A comparative study of Y^{3+}- or/and La^{3+}-doped CeO_2–ZrO_2-based solid solution

Jiaxiu Guo[a)]
College of Architecture and Environment, Sichuan University, Chengdu 610065, China; and National Engineering Research Center for Flue Gas Desulfurization, Chengdu 610065, China

Zhonghua Shi[b)] and Dongdong Wu
College of Chemistry, Sichuan University, Chengdu 610064, China

Huaqiang Yin
College of Architecture and Environment, Sichuan University, Chengdu 610065, China; and National Engineering Research Center for Flue Gas Desulfurization, Chengdu 610065, China

Yaoqiang Chen
College of Chemistry, Sichuan University, Chengdu 610064, China; and National Engineering Research Center for Flue Gas Desulfurization, Chengdu 610065, China

(Received 27 July 2012; accepted 19 December 2012)

$Ce_{0.35}Zr_{0.65-x}RE_xO_2$ (RE = Y and La; $x = 0$ and 0.10) and $Ce_{0.35}Zr_{0.50}Y_{0.075}La_{0.075}O_2$ were prepared by a coprecipitation method. The textures, structures, oxygen storage capacity (OSC), and redox properties of all samples were investigated using Brunauer–Emmett–Teller surface area characterization, x-ray diffraction (XRD), Raman spectra, temperature-programmed technique, and oxygen pulse reaction. The results showed that the fresh $Ce_{0.35}Zr_{0.65}O_2$ has cubic phase, 434 μmol/g of OSC, 82 m^2/g of surface area, and good redox properties; after aging at 1000 °C, $Ce_{0.35}Zr_{0.65}O_2$ still has cubic phase, 418 μmol/g of OSC, and 50 m^2/g of surface area; when Y^{3+} or La^{3+} is added to CeO_2–ZrO_2, the aged $Ce_{0.35}Zr_{0.65-x}RE_xO_2$ (RE = Y and La; $x = 0$ and 0.10) still remains cubic phase, high OSC, and large surface area (47 m^2/g); when Y^{3+} and La^{3+} are simultaneously added into CeO_2–ZrO_2, a stable solid solution with cubic phase is formed and has 459 μmol/g of OSC; and the aged $Ce_{0.35}Zr_{0.50}Y_{0.075}La_{0.075}O_2$ reaches to 60 m^2/g of surface area and has 390 μmol/g of OSC.

I. INTRODUCTION

Nowadays, the environmental protection is receiving much more attention than ever before. One of the major efforts is focused on controlling the emission of toxic pollutants produced during the combustion of fuels in automotive engine. Most of vehicles in the world are equipped with a catalytic converter, which is almost exclusively based on the so-called three-way catalysts (TWC). Generally, a conventional TWC involves two main carriers: oxygen storage materials (ceria-based materials) and supports with high surface area and antisintering at high temperature (such as Al_2O_3, La-stabilized Al_2O_3). Ceria-based solid solutions have been intensively studied for their utilization in TWCs due to the multiple positive effects on the enhancement of catalytic performance. In catalysts, these materials possess large oxygen storage capacity (OSC) and an ability of promoting dispersion of noble metals, promote water-gas shift reaction, and steam reforming reaction and minimize the thermal sintering of alumina supports. But a major drawback of CeO_2 is significant deactivation of the redox couple when it is used at high temperature in the driving conditions, which is attributed to the sintering of CeO_2 particles and the reactions between CeO_2 and γ-Al_2O_3 support or active noble metals.[1,2] For TWC application, the homogeneity and textural stability of the mixed oxide are fairly important. Recently, special attention has been focused on the preparation of CeO_2–ZrO_2 with good thermal stability, excellent redox properties, and high OSC, and the catalytic activity of these materials are strongly enhanced in comparison with pure CeO_2.[3–7] The effect of insertion of ZrO_2 into CeO_2 lattice is clearly confirmed by recent data gathered from literature, and high ZrO_2 content favors the highest textural stability under equivalent synthesis condition.[3,7] Balducci et al.[8,9] have reported that introduction of ZrO_2 into CeO_2 lattice lowers the energy for Ce^{4+} reduction, and with high mobility of lattice oxygen, the diffusion of oxygen from bulk to surface promotes the redox action of Ce^{4+}/Ce^{3+} couples. Further investigation has been showed that Y^{3+} or La^{3+} adding into CeO_2–ZrO_2 can influence the crystalline structure, oxygen mobility, OSC, thermal stability, and redox properties of CeO_2–ZrO_2 solid solutions.[10–13] In our precious study,[14–16] it is found that $Ce_{0.35}Zr_{0.65}O_2$ has excellent texture performance, stable cubic phase, and high OSC, whereas

Address all correspondence to these authors.
[a)]e-mail: guojiaxiu@scu.edu.cn
[b)]e-mail: shizhong95@scu.edu.cn
DOI: 10.1557/jmr.2012.435

 © Materials Research Society 2013

https://doi.org/10.1557/jmr.2012.435 Published online by Cambridge University Press

Y^{3+} or La^{3+} adding into $Ce_{0.35}Zr_{0.65}O_2$ further improves its performance. Recently, Turko et al.[17] have reported that the physicochemical properties of a thermally stable single-phase cerium zirconium oxide with a fluorite structure can be stabilized by Y^{3+} and La^{3+}. To our knowledge, there are few systemic reports on a combined investigation of texture, structure, OSC, and redox properties of CeO_2–ZrO_2–Y_2O_3–La_2O_3 solid solution.

The aim of the present study was to develop a novel oxygen storage material for the removal of toxic pollutants from automotive engine. In this paper, $Ce_{0.35}Zr_{0.65-x}RE_xO_2$ (RE = Y and La; x = 0 and 0.10) and $Ce_{0.35}Zr_{0.50}Y_{0.075}La_{0.075}O_2$ were prepared by a conventional coprecipitation method. The texture, structure, OSC, and redox properties of solid solutions were investigated using Brunauer–Emmett–Teller (BET) surface area characterization, x-ray diffraction (XRD), Raman spectra, and temperature-programmed technique. The OSC of the samples was examined by oxygen pulse reaction.

II. EXPERIMENTAL

A. Materials

Aqueous ammonia (30% NH_3), ammonium carbonate (analytical reagent), and hydrogen peroxide (30%, w/w) were purchased from Chengdu Kelong Chemical Reagent Factory (Chengdu, China). Lanthanum nitrate hexahydrate [$La(NO_3)_3{\cdot}6H_2O$, chemically pure (CP)], cerous nitrate hexahydrate [$Ce(NO_3)_3{\cdot}6H_2O$, CP], yttrium nitrate pentahydrate [$Y(NO_3)_3{\cdot}5H_2O$, CP], and zirconyl nitrate pentahydrate [$ZrO(NO_3)_2{\cdot}5H_2O$, CP] were purchased from Leshan Wutongqiao Dongfeng Chemical Factory, (Leshan, China). All chemicals were used as received without further purification. Distilled water was used throughout the study.

B. Preparation

$Ce_{0.35}Zr_{0.65-x}RE_xO_2$ (RE = Y and La; x = 0 and 0.10) and $Ce_{0.35}Zr_{0.50}Y_{0.075}La_{0.075}O_2$ were prepared by coprecipitation technique. $Ce(NO_3)_3{\cdot}6H_2O$, $ZrO(NO_3)_2{\cdot}5H_2O$, $Y(NO_3)_3{\cdot}5H_2O$, and $La(NO_3)_3{\cdot}6H_2O$ were used as the raw materials. The precursors were mixed in an aqueous solution at the nominal composition with cation concentration of 0.02 mol/L, and an appropriate amount of fresh H_2O_2 (30%) was added to this mixed salt solution. The resulting metal salt solution was simultaneously dropwised to a new container with a mixed solution of ammonia (3 mol/L) and ammonia carbonate aqueous solution (3 mol/L) to reach a pH value of 10. The obtained precipitates were aged at 90 °C for 3 h with vigorous agitation and then filtered. The obtained cake was washed with distilled water until the washing fluid became neutral, subsequently spray dried, and calcined at 600 °C in muffle furnace for 5 h. To compare their thermal stability, the obtained samples were calcined at 1000 °C for 5 h. The resulting powders were in turn tabletted, crushed, and sieved to 40–80 mesh before they were used. $Ce_{0.35}Zr_{0.65}O_2$, $Ce_{0.35}Zr_{0.55}Y_{0.10}O_2$, $Ce_{0.35}Zr_{0.55}La_{0.10}O_2$, and $Ce_{0.35}Zr_{0.50}Y_{0.075}La_{0.075}O_2$ calcined at 600 °C were written as CZ, CZY, CZL, and CZYL. The aged samples were labeled as CZA, CZYA, CZLA, and CZYLA.

C. Characterization

The N_2 adsorption isotherms of the samples at the temperature of liquid nitrogen were obtained on a ZXF-06 automatic surface analyzer (Xibei Chemical Institute, Xianyang, China). All samples were degassed for 1 h at 350 °C in vacuum before commencement of the measurement to remove the surface impurities. The adsorption isotherm data were used to calculate the surface area (S_{BET}) of each sample via the BET equation at relative pressures between 0.05 and 0.35. The crystal structure of the samples was determined by XRD analysis on a computer-controlled DX-1000 diffractometer (Dandong Fangyuan Instrument Co., Dandong, China) using Cu K_α radiation (λ = 0.15406 nm). The x-ray tube was operated at 40 kV and 100 mA. The samples were scanned within the 2θ range of 10–90° at a scanning rate of 0.03°/s. The crystalline phases were identified by comparing them with the reference data from the International Center for Diffraction Data (JPCDS). The laser Raman spectra were recorded using a HORIBA Jobin Yvon LabRAM HR Raman spectrometer (Paris, France) with a 30 mW Ar ion laser (532 nm).

OSC was measured by gas chromatogram in flowing pure N_2 (20 mL/min) on a 200-mg sample at 200 °C. Prior to the OSC measurement, the 200-mg sample was reduced under pure H_2 flow (40 mL/min) from room temperature (RT) to 550 °C and kept at 550 °C for 45 min. And then, the treated sample was cooled to 200 °C under the same conditions and purged with pure N_2. The OSC was measured by injecting pulses of oxygen (82 μmol of O_2) into the sample bed until no oxygen consumption can be detected by a thermal conductivity detector. The temperature-programmed reduction (TPR), oxidation (TPO), and desorption (TPD) experiments were preformed in a quartz tubular microreactor to observe the reductive and oxidative properties of ceria-based solid solutions. Prior to H_2-TPR measurement, the 100-mg sample was pretreated in N_2 with 20 mL/min flow rate from RT to 400 °C with heating rate of 10 °C/min and maintained at 400 °C for 45 min. The treated sample was cooled to RT. The reduction was performed with 5% H_2–95% N_2 mixture at a heating rate of 10 °C/min from RT to 800 °C. The H_2 consumption was monitored by a TCD. After TPR, the samples were cooled to RT in pure N_2 (20 mL/min). And then, the TPO experiments were performed via using a gas 10% O_2–90% N_2 with a flow rate of 20 mL/min, and the

https://doi.org/10.1557/jmr.2012.435 Published online by Cambridge University Press

temperature was heated at a rate of 10 °C/min from RT to 700 °C. The O_2 consumption was measured by a TCD. Before performing an O_2-TPD experiment, the 100-mg sample was first pretreated in pure N_2 with a flow rate of 20 mL/min at 400 °C for 45 min, and then, the gas flow was switched to 10% O_2–90% N_2 with a flow rate of 20 mL/min at 400 °C for 45 min. Finally, the sample was cooled to RT in the same atmosphere. After being cooled to RT, the sample was heated at a rate of 10 °C/min from RT to 600 °C in pure N_2 (20 mL/min) for O_2 desorption. The effluent gas was monitored online by a TCD.

III. RESULTS

A. Textural properties and phase structure of the solid solutions

The textural properties of all samples before and after aging at 1000 °C are summarized in Table I. When Y^{3+} or La^{3+} is added to CeO_2–ZrO_2, the pore volume of both samples slightly decreases. The surface area of CZL reaches to 92 m^2/g, and the surface area and pore volume of CZYL increase to 105 m^2/g and 0.27 mL/g, respectively. The average pore radius of CZ, CZY, and CZL is 8.3, 5.0, and 5.6 nm, respectively, whereas that of CZYL is 9.0 nm. After aging at 1000 °C for 5 h, the surface area, average pore radius, and pore volume of all samples undergo a decrease, but CZYLA still has 60 m^2/g of surface area, 9.6 nm of average pore radius, and 0.13 mL/g of pore volume, indicating that some synergic effects of Y^{3+} and La^{3+} significantly enhance textural stability of CeO_2–ZrO_2.

The XRD patterns of La_2O_3, Y_2O_3, CZ, CZY, CZL, and CZYL are shown in Fig. 1. The diffraction peaks at 26.18°, 29.18°, 30.08°, 39.58°, 46.18°, 52.18°, 52.93°, 55.54°, 55.39°, 60.19°, 62.32°, 66.94°, 71.92°, 75.31°, 80.74°, 83.56°, and 84.28° are due to hexagonal structure of La_2O_3 (JCPDS Card No. 74-2430). The XRD pattern of Y_2O_3 powders exhibits the cubic structure, and the diffraction peaks are at 2θ = 20.47°, 29.20°, 33.85°, 35.89°, 39.73°, 43.66°, 48.61°, 53.35°, 57.64°, 60.64°, 77.68°, 71.17°, 77.89°, and 81.01°, which is in good agreement with the pattern in JCPDS File No. 83-0927. The broadening of the reflections in the diffractograms distinctly indicates its nanocrystalline nature. It is revealed that all samples calcined at 600 °C are nanocrystalline with about 5 nm size calculated from XRD peak-broadening analysis (Table I). For CZ, the obvious peaks at 2θ = 29.56°, 34.3°, 49.15°, 58.48°, 61.90°, 72.67°, 79.93°, and 82.54° [Fig. 1(a)] are observed. When Y^{3+} is induced into CeO_2–ZrO_2, a new solid solution is formed, whereas the diffraction peaks (2θ) [Fig. 1(b)] shift to 29.14°, 34.03°, 48.46°, 57.22°, 60.7°, 71.20°, 78.86°, and 81.43°. Similar profiles are also obtained from the others. The diffraction peaks (2θ) of CZL [Fig. 1(c)] are 29.20°, 33.73°, 48.61°, 57.85°, 60.82°, 71.56°, 78.64°, and 81.04°. The broadest diffraction peaks of CZYL [Fig. 1(d)] are attributed to the presence of small crystallites (4.8 nm) effect, and the diffraction peaks are 29.29°, 34.15°, 49.48°, 58.51°, 60.94°, 71.62°, 78.58°, and 81.10°. These results indicate that Y^{3+} or/and La^{3+} can enter into the CeO_2–ZrO_2 lattice.

The structural homogeneity and thermal stability of the prepared materials are performed by the following calcination at high temperature. All samples are calcined at 1000 °C for 5 h, and the nature of phase is examined. The XRD patterns are reported in Fig. 2. No asymmetric

TABLE I. Surface area (*S*), average pore radius (*R*), average particle size (*P*), pore volume (V), and OSC.

Samples	*S* (m^2/g)	*R* (nm)	*P*[a] (nm)	*V* (mL/g)	OSC (μmol/g)
CZ	82	8.3	5.5	0.18	434
CZY	82	5.0	5.0	0.13	384
CZL	92	5.6	5.3	0.13	396
CZYL	105	9.0	4.8	0.27	459
CZA	50	7.7	10.5	0.10	418
CZYA	47	8.2	10.1	0.08	313
CZLA	48	9.3	7.3	0.12	318
CZYLA	60	9.6	7.0	0.13	390

[a]Estimated according to XRD peak-broadening analysis.

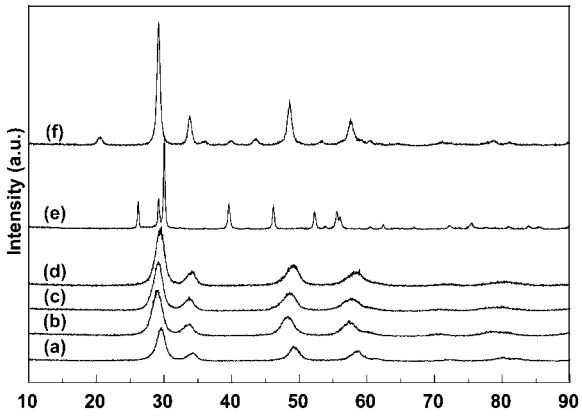


FIG. 1. XRD patterns of CZ (a), CZY (b), CZL (c), CZYL (d), La_2O_3 (e), and Y_2O_3 (f).

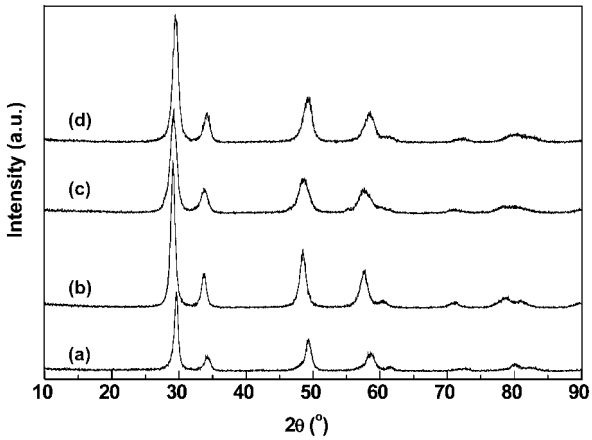


FIG. 2. XRD patterns of aged CZA (a), CZYA (b), CZLA (c), and CZYLA (d).

https://doi.org/10.1557/jmr.2012.435 Published online by Cambridge University Press

peaks are found in the XRD patterns of all samples, indicating that the prepared materials could form a single-phase solid solutions. And the width of all XRD peaks become narrow, which is an indication that all samples occur sintering [compared with Figs. 1(a)–1(d) and the average particle size of the solids increases (Table I)]. However, the prepared materials containing La^{3+} still maintain nanometeric level, 7.3 nm for CZLA and 7.0 nm for CZYLA, indicating that La^{3+} could better efficiently retard CeO_2–ZrO_2 crystal sintering and particles growth. From phase analysis, the obvious diffraction peaks of CZA at 2θ = 29.62°, 34.51°, 49.39°, 58.57°, 61.90°, 72.85°, 80.38°, and 82.87° are observed. When Y^{3+} or La^{3+} is induced into CeO_2–ZrO_2, the diffraction peaks of CZYA shift to 29.11°, 33.85°, 48.52°, 57.76°, 60.79°, 71.53°, 79.12°, and 81.64°, and those of CZLA shift to 29.23°, 34.00°, 48.73°, 57.97°, 61.57°, 71.44°, 79.03°, and 80.86°. When Y^{3+} and La^{3+} are simultaneously added to CeO_2–ZrO_2, the diffraction peaks of ZYLA at 29.44°, 34.24°, 49.54°, 58.55°, 61.45°, 72.43°, 80.62°, and 82.51° are detected. These results indicate that Y^{3+} or/and La^{3+} effectively stabilize the phase of materials and significantly improve thermal stability.

The Raman spectra can be used to confirm the structure of the solid solutions. The Raman spectra of the prepared materials, La_2O_3 and Y_2O_3. are illustrated in Fig. 3. The Raman bands at 104, 190, and 407 cm^{-1} are assigned to La_2O_3 and bands at 130, 162, 194, 245, 318, 331, 377, 420, 431, 470, 508, 560, 594, 645, 734, 815, and 970 cm^{-1} are assigned to Y_2O_3. All fresh samples have one strong Raman peak at ~471 cm^{-1} and weak peak at ~627 cm^{-1}, indicating that Y^{3+} and/or La^{3+} enter into the CeO_2–ZrO_2 lattice. The former is due to F_{2g} mode of c-CeO_2, and the latter is attributed to the presence of intrinsic O vacancies in the lattice.[18] After aging at 1000 °C

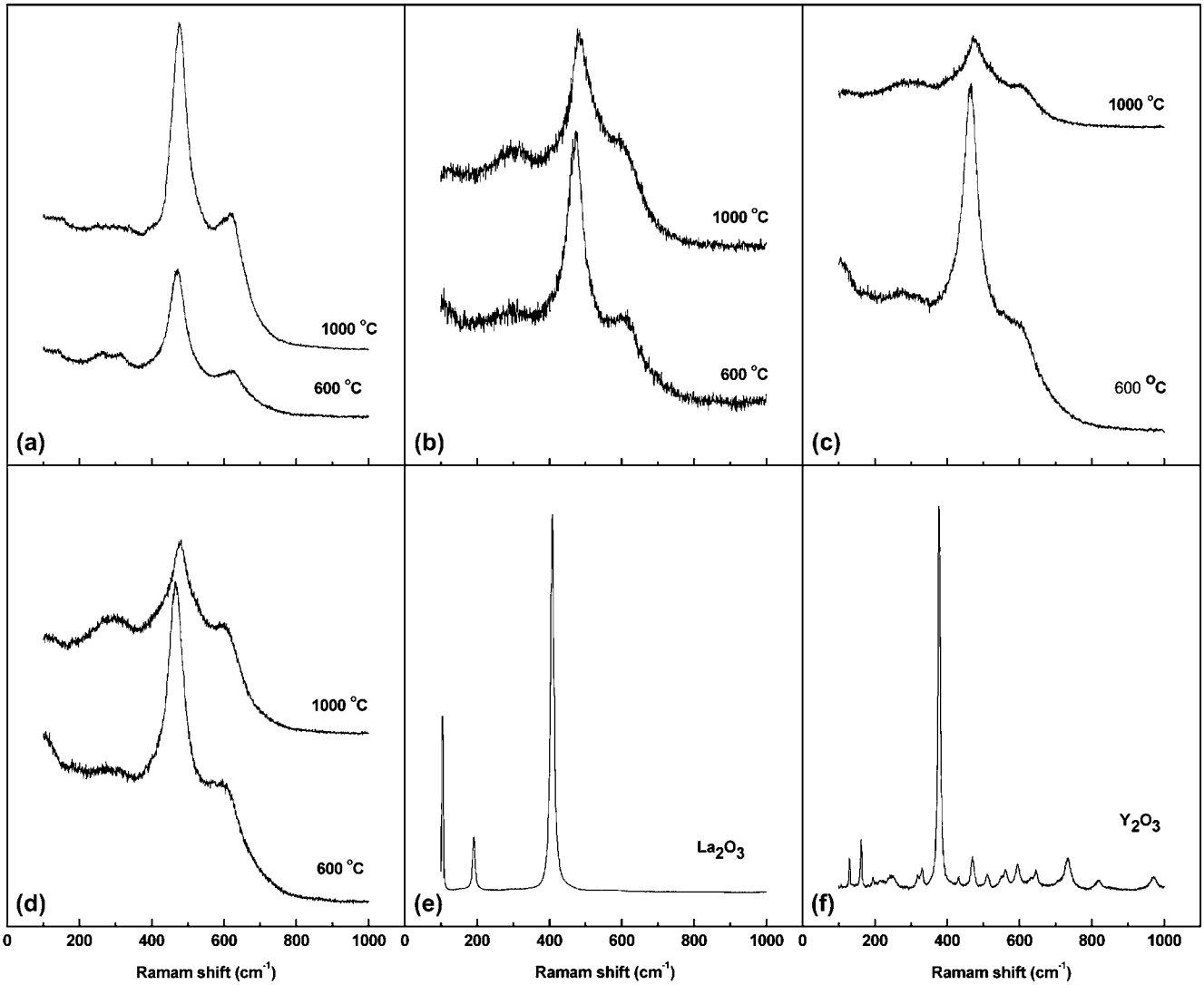


FIG. 3. Raman spectra of CZ (a), CZY (b), CZL (c), CZYL (d), La_2O_3 (e), and Y_2O_3 (f).

https://doi.org/10.1557/jmr.2012.435 Published online by Cambridge University Press

for 5 h, one strong Raman peak at ~474 cm^{-1} and a broad weak peak at ~628 cm^{-1} are observed for aged CZ, indicating that CeO_2–ZrO_2 can form a stable cubic phase under our experimental condition. When Y^{3+} is induced into CeO_2–ZrO_2, one strong Raman peak at ~478 cm^{-1}, a broad weak peak at ~300 cm^{-1}, and a weak peak at ~605 cm^{-1} are observed. For aged CZL, there are a strong Raman peak at ~472 cm^{-1} and two broad weak peaks at ~300 and 605 cm^{-1}. When Y^{3+} and La^{3+} are simultaneously added to CeO_2–ZrO_2, a strong Raman peak at ~481 cm^{-1}, a weak peak at ~605 cm^{-1}, and a broad peak at ~300 cm^{-1} are observed. These results indicate that Y^{3+} and/or La^{3+} do not segregate from the CeO_2–ZrO_2 solid solution after aging at 1000 °C.

B. OSC and redox behaviors

The OSC and redox properties of the sample used in this work are investigated by oxygen pulse reaction and temperature-programmed technique, respectively. The H_2-TPR profiles of fresh samples are illustrated in Fig. 4. Yao and Yao[19] have found that a new oxygen species, probably a molecular oxygen anion, is formed at 25 °C, which converts slowly at 500 °C to the capping oxygen anion, and complete restoration of all three types of oxygen anions is accomplished at 850 °C in air. The reduction peaks of the surface capping oxygen and the bulk oxygen of CeO_2 are centered at 500 and 800 °C,[19] respectively. Zhu et al.[20] have found that the reduction of CeO_2 starts at 280 °C and two broad peaks are observed at 510 and 800 °C, respectively. The peak at 510 °C is assigned to the reduction of surface capping oxygen of CeO_2, and the peak at 800 °C can be attributed to the reduction of bulk CeO_2. Teng et al.[21] have reported that two reduction peaks (420 and 567 °C) of m-$Ce_{0.8}Zr_{0.2}O_2$ correspond to the reduction of oxygen from surface and bulk ceria, respectively. He et al.[22] have found that Y^{3+} doping into the CeO_2–ZrO_2 lattice can increase the concentrations of oxygen vacancies and Ce^{3+} ions, and the reduction peaks at ~528 and 825 °C in the first TPR run are observed. The peak at around 400 °C is ascribed to the reduction of surface capping oxygen (O^{2-}, O) species due to the defects of structure and electronic properties of nonstoichiometric ceria.[23] For CZ, a single broad reduction peak centered at 580 °C is observed. For CZY, a broad reduction peak at 562 °C with two small peaks at 180 and 218 °C (local) are observed, indicating that there are at least two types of adsorbed surface oxygen species located at lower temperatures and the reduction peak centered at 562 °C could be assigned to the Ce^{4+} reduction of surface or subsurface. For CZL, the reduction peak centered at 608 °C is due to the reduction of Ce^{4+} located on the surface (subsurface), and the reduction peaks at 270 and 294 °C are attributed to the adsorbed oxygen species on the surface. There are three separate reduction peaks at 298, 323, and 615 °C for CZYL, suggesting that the reduction at the higher temperature belongs to the Ce^{4+} located on the surface (subsurface), whereas the reduction at the lower temperature is probably adsorbed oxygen species. These results indicate that the introduction of trivalent dopants (Y^{3+} or/and La^{3+}) to the CeO_2–ZrO_2 solid solution can change the surface chemical property of solid solution, which increases the adsorption capacity of oxygen species on the surface of solid solution.

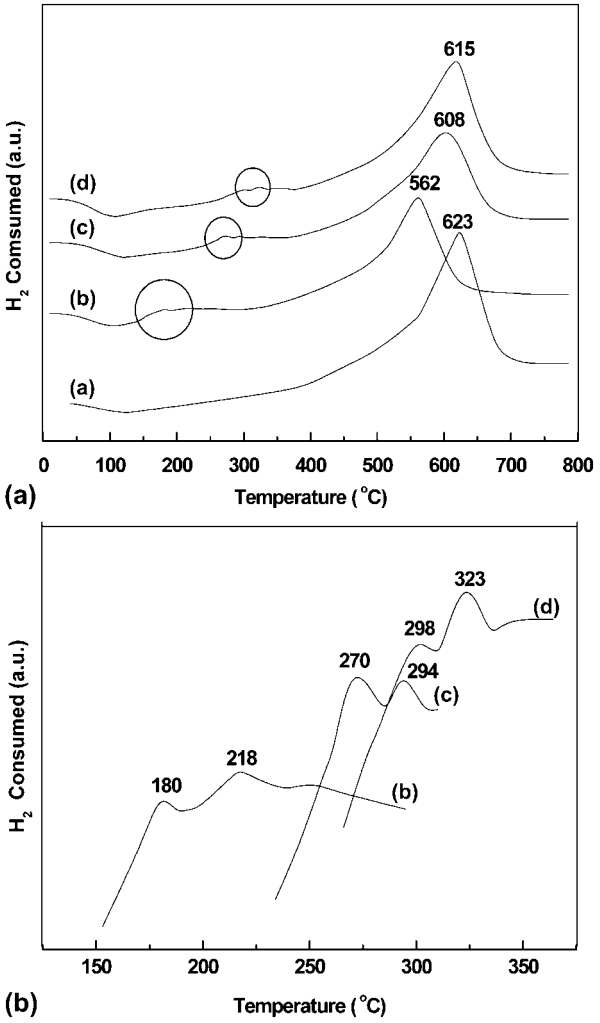


FIG. 4. H_2-TPR profiles of fresh CZ (a), CZY (b), CZL (c), and CZYL (d) samples; (A) whole, (B) local (○).

All samples are measured by O_2-TPO after TPR to obtain a deeper insight into the reoxidation property. The O_2-TPO profiles of CZ, CZY, CZL, and CZYL are illustrated in Fig. 5. There is only one oxidation peak at 96 °C for CZ, indicating that only a surface Ce^{3+} is oxidized to Ce^{4+}. For CZY, two oxidation peaks at 83 and 293 °C are observed, suggesting that the surface Ce^{3+} is oxidized to Ce^{4+} at 83 °C and the oxidation peak at 293 °C belongs to the oxidation of subsurface Ce^{3+}. For CZL, there are two oxidation peaks at 97 and 411 °C. They belong to the

https://doi.org/10.1557/jmr.2012.435 Published online by Cambridge University Press

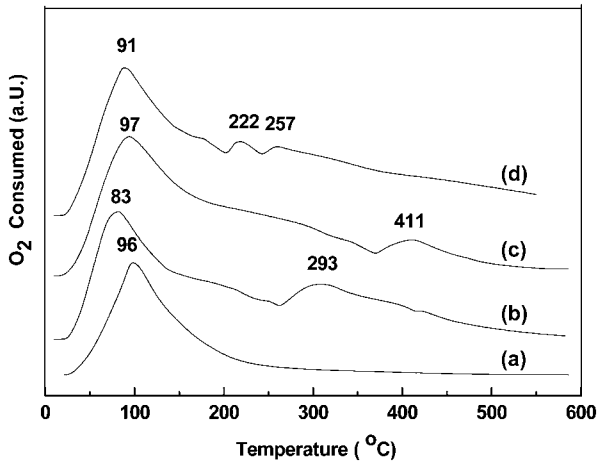


FIG. 5. O_2-TPO profiles of CZ (a), CZY (b), CZL (c), and CZYL (d) samples.

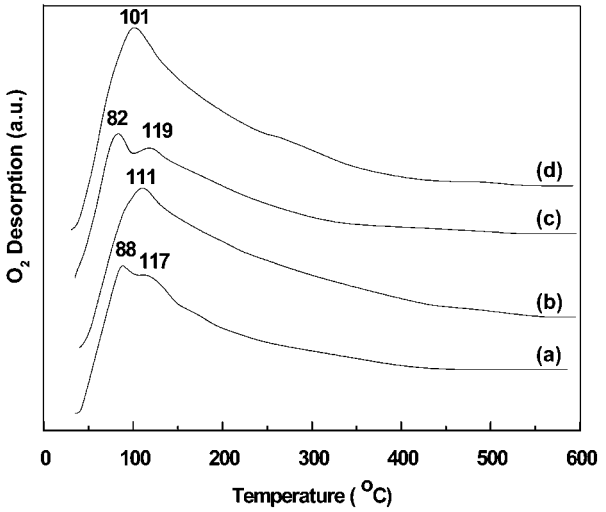


FIG. 6. O_2-TPD profiles of fresh CZ (a), CZY (b), CZL (c), and CZYL (d) samples.

Ce^{3+} oxidation of surface and subsurface, respectively. Three oxidation peaks at 91, 222, and 257 °C for CZYL are observed, showing that the surface Ce^{3+} is oxidized to Ce^{4+} at 91 °C and the presence of Ce^{3+} oxidation peaks at 222 and 257 °C due to the subsurface Ce^{3+}. These results show that when Y^{3+} and La^{3+} are simultaneously induced to CeO_2–ZrO_2, the oxygen mobility increases from surface to bulk, which is in favor of oxygen migration.

The O_2-TPD profiles of the prepared materials are shown in Fig. 6. According to the literature,[24,25] in O_2-TPD curves, two desorption peaks are usually observed that the low temperature peak ($T < 400$ °C) represents the desorption of oxygen adsorbed on the surface oxygen vacancies, such as the species O^{2-} and O^-, and the high temperature peak ($T > 400$ °C) is considered as coming from the bulk of the solid.[26] One desorption peak at 88 °C and a shoulder at 117 °C are observed for CZ. With the incorporation of Y^{3+} into the CZ lattice, there is a large peak centered at 111 °C [Fig. 6(b)]. When La^{3+} is incorporated into the CeO_2–ZrO_2, there are two desorption peaks at 82 and 119 °C [Fig. 6(c)]. For CZYL, a large broad peak centered at 101 °C is observed. This indicates that Y^{3+} and La^{3+} are simultaneously induced into the CeO_2–ZrO_2 lattice resulting in the increase of oxygen adsorbed capacity.

The oxygen pulse technique is used to study the OSC of samples, and the results are summarized in Table I. It is reported by Vidal et al.[27] that the OSC of $Ce_{0.15}Zr_{0.85}$ has 260 μmol/g at 427 °C measurement and that of $Ce_{0.50}Zr_{0.50}$ has 740 μmol/g. In our previous study,[14] the OSC of $Ce_{0.50}Zr_{0.50}$ before and after aging at 1000 °C has 414 and 268 μmol/g at 200 °C, respectively. The OSC of CZ, CZY, CZL, and CZYL at 200 °C are 435, 384, 396, and 460 μmol/g, respectively. After aging at 1000 °C for 5 h, the OSC of all samples are in decrease, but CZYLA still possesses 390 μmol/g, showing that the Y^{3+} and La^{3+} coincorporation into the CeO_2–ZrO_2 increases the OSC compared to CZYA and CZLA. In a summary, the OSC of fresh samples follows a sequence of CZY < CZL < CZ < CZYL and that of aged samples is CZYA < CZLA < CZYL < CZ.

IV. DISCUSSION

A. Defective structure and textural properties

In previous research, it has been observed that pure CeO_2 (JCPDS Card No. 43-1002[28]) has the fluorite structure. When ZrO_2 is inserted into the CeO_2 framework, CeO_2–ZrO_2 mixed oxides have a quite complex phase diagram, containing three stable phases [monoclinic, tetragonal (t), and cubic] and two metastable phases (t' and t''). The t phase is formed through a decomposition of the diffused phases, whereas the t' phase is obtained through a diffusion transition. The t'' phase is an intermediate phase between t' and cubic CeO_2 and is very close to the fluorite cubic structure except that there is the displacement of the oxygen atom in its crystal lattice.[29,30] In the intermediate domain, the true nature of CeO_2–ZrO_2 phase diagram is still unidentified due to the presence of many stable and metastable tetragonal phases.[30–32] It is generally accepted that the crystal structure of a CeO_2–ZrO_2 solid solution depends on chemical composition and synthesis procedure. Nakatani et al.[31] has reported that the amount of monoclinic ZrO_2 decreases and metastable tetragonal ZrO_2 appears when the content of CeO_2 increases from 0 to 20 mol%. But when CeO_2 content is above 80 mol%, there is only one cubic phase. Given the relatively large difference (13%) between the cation radius of Ce^{4+} (0.097 nm) and Zr^{4+} (0.084 nm), a limited mutual solubility might be expected. The bulk $Ce_{1-x}Zr_xO_2$ ($\chi = 0.4$–0.65) materials exhibit the t' phase at RT in previous report.[30,33] It has been established that

https://doi.org/10.1557/jmr.2012.435 Published online by Cambridge University Press

six Raman-active modes of $A_{1g} + 3E_g + 2B_{1g}$ symmetry are observed for tetragonal ZrO_2 (space group $P4_2/nmc$), while for the cubic fluorite structure (space group $Fm3m$), only one F_{2g} mode centered at around 465 cm^{-1} is Raman active for CeO_2.[30,34] The weak peaks at ~620 (Ref. 18) and 600 cm^{-1} (Ref. 35) are attributed to the intrinsic O vacancies in the lattice. The Raman peak at ~315 cm^{-1} indicates a metastable phase (t″) in CeO_2–ZrO_2 materials.[36] The appearance of weak bands at ~300 cm^{-1} could be attributed to the displacement of the O atoms from their ideal fluorite lattice position.[37] Raman bands at 403, 186, and 102 cm^{-1} are assigned to La_2O_3 and bands at 131, 163, 196, 318, 332, 379, 433, 470, and 585 cm^{-1} belong to Y_2O_3.[38] In Fig. 1, no phase segregation is observed, and a stable solid solution is formed under the conditions adopted in our work for CeO_2–ZrO_2-based material preparation. For fresh $Ce_{0.35}Zr_{0.65}O_2$, the diffraction peaks are close to cubic phase of CeO_2 (JPCDS Card No. 43-1002), indicating that fresh $Ce_{0.35}Zr_{0.65}O_2$ solid solutions show a face-centered cubic lattice structure at ambient conditions. It is reported that the addition of Y^{3+} stabilizes the cubic structure of ternary systems at very low content of both yttrium and cerium oxides (less than 10 mol%).[39] Kulyova et al.[40] have also found that $Y_{0.1}Ce_{0.1}Zr_{0.8}O_2$ possesses a stable cubic phase. In our experiment, when Y^{3+} or/and La^{3+} are incorporated into CeO_2–ZrO_2 with 35 mol% CeO_2 content, a single cubic phase is detected and no phase separation is observed. For all fresh samples in Fig. 3, the Raman peaks at ~472 and 627 cm^{-1} are respectively attributed to F_{2g} mode of c-CeO_2 and the presence of defective structure. It is confirmed that the as-prepared CeO_2–ZrO_2-based materials form a single cubic phase. For all aged samples, no phase segregation is observed (in Fig. 2), but the corresponding sample shows a different Raman shift (in Fig. 3), indicating that CeO_2–ZrO_2-based materials have different structure, which cannot be distinguished in the XRD. For aged $Ce_{0.35}Zr_{0.65}O_2$, one strong Raman peak at ~474 cm^{-1} and a broad weak peak at ~628 cm^{-1} are observed for aged CZ. The former is attributed to F_{2g} mode of c-CeO_2, and the latter is due to the presence of intrinsic O vacancies, indicating that CeO_2–ZrO_2 can form a stable cubic phase under our experimental condition. When Y^{3+} or/and La^{3+} are added to CeO_2–ZrO_2, no new phase is observed and the displacement of the O atoms from their ideal fluorite lattice position is increased. In our studies, the diffraction peaks of La_2O_3 and Y_2O_3 are not detected in XRD characterization, and Raman spectra of La_2O_3 and Y_2O_3 are not observed. This result implies that Y^{3+} or/and La^{3+} increase the defective structure of CeO_2–ZrO_2. In Table I, the prepared materials containing La^{3+} have small particle size (7.3 nm for CZL and 7.0 nm for CZYL) after high temperature (1000 °C), indicating that La^{3+} can significantly improve thermal stability. When small Y^{3+} is introduced into the CeO_2–ZrO_2–La_2O_3, the face-centered cubic phase of CeO_2–ZrO_2 is more stable at high temperature treatment for long time. This result indicates that Y^{3+} or/and La^{3+} enter into CeO_2–ZrO_2 crystal lattice, which can significantly increase phase homogeneity, defective structure, and high thermal stability.

The performance of catalysts depends on the phase composition, homogeneity, and surface area of powders.[41] Furthermore, high surface area, appreciable pore volume, and high calcination temperatures may be used to obtain an efficient incorporation of both ZrO_2 and trivalent dopants (such as Y^{3+} and La^{3+}) into the CeO_2 lattice. The first two properties would be very important for noble metal deposition in the preparation of TWCs. In Table I, there are only slightly changes about surface area of the samples containing 10 mol% Y^{3+} or La^{3+}. The dopants with 7.5 mol% Y^{3+} and 7.5 mol% La^{3+} are conducive to form a single cubic phase and significantly increase the surface area, indicating that there are some synergistic effects of Y^{3+} and La^{3+} because they have near ionic radii (Y^{3+} 0.110 nm and La^{3+} 0.118 nm) in the solid solution formation process.

B. Oxygen storage and redox behavior

In Table I, the OSC of CZ is 434 μmol/g and higher than that of CZY (384 μmol/g) and CZL (396 μmol/g) but less than that of CZYL (456 μmol/g). This represents a mechanism for the release of the stress generated by insertion of the smaller Zr^{4+} (0.084 nm) into the CeO_2 lattice, and at the same time, it is responsible for the high oxygen mobility in the bulk by generating mobile oxygen in the lattice itself. Because Y^{3+} (0.110 nm) and La^{3+} (0.118 nm) are close to Ce^{4+} (0.101 nm), Y^{3+} or La^{3+} may easily compete with Ce^{4+} for the low coordinated sites, not allowing an efficient release of the stress in the lattice. This is not conducive to the movement of oxygen in the bulk. The face-centered cubic lattice is described as oxygen ions occupying the empty of tetrahedral interstitial sites and octahedral sites in a perfect fluorite structure.[42] The OSC of ceria-based oxides is not correlated with the surface area but depends on the concentration of oxygen defect.[42] The crystal lattice of CZYL is close to the face-centered cubic lattice of CZ, and their OSC is also very close. This explains that the OSC of materials is more determined by the oxygen-defective structure, whereas the external texture is not the key factor for governing the OSC performance of the prepared CeO_2–ZrO_2-based solid solution.

The TPR profiles of the prepared materials show a single, slightly asymmetric, and reduction peak centered at about 600 °C. In the XRD characterization and Raman spectra, the fresh materials display a single stable face-centered cubic nanostructure. This evidence indicates that TPR profiles of ceria–zirconia oxides with single phase generally display a single reduction peak.[43] In Fig. 4, the small shifts of the reduction peaks in the fresh samples

https://doi.org/10.1557/jmr.2012.435 Published online by Cambridge University Press

could be related with the increase of oxygen mobility by the dopants. The reductive behavior of CeO_2–ZrO_2-based solid solution is strongly affected by the temperature of the preoxidation performed before the TPR run: a mild oxidation generates a low temperature reduction profile, whereas the severe high temperature oxidation generates high temperature reduction profiles.[44] In our work, the reduction peak of all samples is occurring around 600 °C. That is because the samples are only pretreated in pure N_2 at 400 °C for 45 min before TPR and the chemical environment of reductive species on the samples are not changed. Compared with the reduction peak of $Ce_{0.35}Zr_{0.65}O_2$, the reduction peak of solids doping with Y^{3+}, La^{3+} and Y^{3+}, and La^{3+} is performed at less than 61, 15, and 8 °C, respectively, suggesting that CZY is the most easy to release oxygen so that it has the lowest reduction temperature compared to CZL and CZYL (Fig. 4). Oxygen vacancies in the defective structures of CZY, CZL, and CZYL are believed to be responsible for the good performance in O_2 oxidation at low temperature (Fig. 5) and for the high tendency of oxygen diffusion (Fig. 6). In the TPR of fresh sample, there are a collapse of surface area and a filling of pore, which can hinder the concomitant reduction of the surface. Conversely, the different initial texture of the solid solution modifies the reduction temperatures in the TPR and affects the behavior in the TPO (Fig. 5).

C. Oxygen mobility

Oxygen mobility is an important factor to consider when solid oxides are used as catalysts in the oxidation of carbon monoxide and hydrocarbons and in the removal of automotive exhaust. Generally, there are several oxygen adsorbed species such as O_2^-, O_2^{2-}, and O^- on the surface of an oxygen-containing catalyst. Semiconductor oxides and some metal surface can adsorb O_2 (including some O_2^-) at the lower temperature, while at higher temperatures, O_2 or O_2^- is dissociated into O^- and adsorbed on the oxide surface. The order of the adsorption energy of the three kinds of particles is $O_2 < O_2^- < O^-$. Liotta et al.[45] have found that a sharp peak of physisorbed O_2 is observed at 50 °C. Superoxide (O^{2-}) and/or peroxide (O_2^{2-}) species are transiently produced by oxygen adsorption on the surface reduced defects formed under vacuum already at 200 °C or upon thermal treatment at higher temperatures.[46] From the O_2-TPD, the prepared materials should be expected to exhibit significant differences in their structural and chemical surface properties, which may lead to a distinct capability for activating the dioxygen molecule. Oxygen adsorbed on the surface of the prepared materials exhibits different desorption temperature, showing that there are several different active oxygen species. CZ and CZL have two desorption peaks [Figs. 6(a) and 6(c)], showing that two active oxygen species exist on the surface. One broad peak of CZY and CZYL is observed [Figs. 6(b) and 6(d)], indicating that one active oxygen species locates on the surface of solid solution. The first TPD peak corresponds to the existence of O_2^- ions, which is nested in surface oxygen vacancies presented in the prepared CeO_2–ZrO_2-based solid solution. From the profiles of O_2-TPD, it can be concluded that the introduction of Y^{3+} into CeO_2–ZrO_2 lattice can increase surface oxygen vacancies, which is consistent with the literature.[22] When La^{3+} is added to CeO_2–ZrO_2 lattice, there are two types of superoxide species on the surface. These oxygen species can intertransform via a sequence of $O_2^- \Leftrightarrow O_2^{2-} \Leftrightarrow O^- \Leftrightarrow O_{lattice}^{2-}$ at elevated temperatures. In this study, it is suggested that the oxygen mobility of CeO_2–ZrO_2-based solid solution may increase the available surface oxygen to enhance the surface oxidation reaction (Fig. 5). The characterization results of TPO and TPD reveal that the presence of Y^{3+} and La^{3+} in the CeO_2–ZrO_2 framework increases the oxygen mobility.

V. CONCLUSIONS

In summary, the present investigation has an important role of trivalent dopants in proving the oxygen storage at low temperatures in the CeO_2–ZrO_2. In our work, $Ce_{0.35}Zr_{0.50}Y_{0.075}La_{0.075}$ with high OSC at low temperatures is prepared by a simple coprecipitation method. The insertion of trivalent cation (Y^{3+} and La^{3+}) into CeO_2–ZrO_2 significantly improves textural and structural properties, and most importantly, it favors the homogeneity of face-centered cubic phases and high thermal stability. A hinder thermal deactivation should be achieved under the real exhaust conditions. $Ce_{0.35}Zr_{0.50}Y_{0.075}La_{0.075}$ can become new generation oxygen storage material and be widely used in TWCs. This novel oxygen storage material can be satisfied with rigorous emission regulations of vehicle exhaust.

ACKNOWLEDGMENTS

This project is financially supported by the National Nature Science Youth Fund of China (Grant No. 21173153). We would like to thank Professor Zhu, College of Materials Science and Engineering, Sichuan University for XRD measurements, and Dr. Wu, Analytical and Testing Center, Sichuan University for Raman spectra characterization.

REFERENCES

1. H.S. Gandhi and M. Shelef: The role of research in the development of new generation automotive catalysts. *Stud. Surf. Sci. Catal.* **30**, 199–214 (1987).
2. G. Kim: Ceria-promoted three-way catalysts for auto exhaust emission control. *Ind. Eng. Chem. Prod. Res. Dev.* **21**, 267–274 (1982).
3. M. Pijolat, M. Prin, M. Soustelle, O. Touret, and P. Nortier: Thermal stability of doped ceria: Experiment and modeling. *J. Chem. Soc., Faraday Trans.* **91**, 3941–3948 (1995).
4. P. Fornasiero, R. Di Monte, G. Ranga Rao, J. Kašpar, S. Meriani, A. Trovarelli, and M. Graziani: Rh-loaded CeO_2-ZrO_2 solid-solutions

https://doi.org/10.1557/jmr.2012.435 Published online by Cambridge University Press

as highly efficient oxygen exchangers: Dependence of the reduction behavior and the oxygen storage capacity on the structural-properties. *J. Catal.* **151**, 168–177 (1995).
5. T. Murota, T. Hasegawa, S. Aozasa, H. Matsui, and M. Motoyama: Production method of cerium oxide with high storage capacity of oxygen and its mechanism. *J. Alloys Compd.* **193**, 298–299 (1993).
6. S. Rossignol, Y. Madier, and D. Duprez: Preparation of zirconia-ceria materials by soft chemistry. *Catal. Today* **50**, 261–270 (1999).
7. J. Kašpar, R. Di Monte, P. Fornasiero, M. Graziani, H. Bradshaw, and C. Norman: Dependency of the oxygen storage capacity in zirconia–ceria solid solutions upon textural properties. *Top. Catal.* **16–17**, 83–87 (2001).
8. G. Balducci, J. Kašpar, P. Fornasiero, M. Graziani, M.S. Islam, and J.D. Gale: Computer simulation studies of bulk reduction and oxygen migration in CeO_2-ZrO_2 solid solutions. *J. Phys. Chem. B* **101**, 1750–1753 (1997).
9. G. Balducci, J. Kašpar, P. Fornasiero, M. Graziani, and M.S. Islam: Surface and reduction energetics of the CeO_2-ZrO_2 catalysts. *J. Phys. Chem. B* **102**, 557–561 (1998).
10. L.N. Ikryyannikova, A.A. Aksenov, G.L. Markaryan, G.P. Muravieva, B.G. Kostyuk, A.N. Kharlanov, and E.V. Lunina: The red-ox treatments influence on the structure and properties of M_2O_3-CeO_2-ZrO_2 (M = Y, La) solid solutions. *Appl. Catal., A* **210**, 225–235 (2010).
11. H. He, H.X. Dai, and C.T. Au: Defective structure, oxygen mobility, oxygen storage capacity, and redox properties of RE-based (RE = Ce, Pr) solid solutions. *Catal. Today* **90**, 245–254 (2004).
12. H. He, H.X. Dai, L.H. Ng, K.W. Wong, and C.T. Au: Pd-, Pt-, and Rh-loaded $Ce_{0.6}Zr_{0.35}Y_{0.05}O_2$ three-way catalysts: An investigation on performance and redox properties. *J. Catal.* **206**, 1–13 (2002).
13. P. Vidmar, P. Fornasiero, J. Kaspar, G. Gubitosa, and M. Graziani: Effects of trivalent dopants on the redox properties of $Ce_{0.6}Zr_{0.4}O_2$ mixed oxide. *J. Catal.* **171**, 160–168 (1997).
14. J.X. Guo, D.D. Wu, L. Zhang, M.C. Gong, M. Zhao, and Y.Q. Chen: Preparation of nanometric CeO_2-ZrO_2-Nd_2O_3 solid solution and its catalytic performances. *J. Alloys Compd.* **460**, 485–490 (2008).
15. J.X. Guo, S.H. Yuan, M.C. Gong, M. Shen, J.B. Zhong, and Y.Q. Chen: Influence of $Ce_{0.35}Zr_{0.55}Y_{0.10}$ solid solution on performance of Pt-Rh three-way catalysts. *J. Rare Earths* **25**, 179–183 (2007).
16. J.X. Guo, S.H. Yuan, M.C. Gong, L. Zhang, D.D. Wu, M. Zhao, and Y.Q. Chen: Influence of $Ce_{0.35}Zr_{0.55}La_{0.10}O_{1.95}$ solid solution on the performance of Pt-Rh three-way catalysts. *Acta Phys. Chim. Sin.* **23**, 73–78 (2007).
17. G.A. Turko, A.S. Ivanva, L.M. Plyasova, G.S. Litvak, and V.A. Rogov: Synthesis and characterization of fluorite-like Ce-Zr-Y-La-O systems. *Kinet. Catal.* **46**, 884–890 (2005).
18. J.R. McBride, K.C. Hass, B.D. Poindexter, and W.H. Weber: Raman and X-ray studies of $Ce_{1-x}RE_xO_{2-y}$, where RE=La, Pr, Nd, Eu, Gd and Tb. *J. Appl. Phys.* **76**, 2435–2441 (1994).
19. H.C. Yao and Y.F.Y. Yao: Ceria in automotive exhaust catalysts: I. Oxygen storage. *J. Catal.* **86**, 254–265 (1984).
20. H. Zhu, Z. Qin, W. Shan, W. Shen, and J. Wang: Pd/CeO_2–TiO_2 catalyst for CO oxidation at low temperature: A TPR study with H_2 and CO as reducing agents. *J. Catal.* **225**, 267–277 (2004).
21. M. Teng, L. Luo, and X. Yang: Synthesis of mesoporous $Ce_{1-x}Zr_xO_2$ (x = 0.2-0.5) and catalytic properties of CuO based catalysts. *Microporous Mesoporous Mater.* **119**, 158–164 (2009).
22. H. He, H.X. Dai, K.W. Wong, and C.T. Au: $RE_{0.6}Zr_{0.4-x}Y_xO_2$ (RE = Ce, Pr; x = 0, 0.05) solid solutions: An investigation on defective structure, oxygen mobility, oxygen storage capacity, and redox properties. *Appl. Catal., A* **251**, 61–74 (2003).
23. C. Li, G. Zhou, L. Wang, S. Dong, J. Li, and T. Cheng: Effect of ceria on the MgO-γ-Al_2O_3 supported $CeO_2/CuCl_2$/KCl catalysts for ethane oxychlorination. *Appl. Catal., A* **400**, 104–110 (2011).
24. Y. Teraoka, M. Yoshimatsu, N. Yamazoe, and T. Seiyama: Oxygen-sorptive properties and defect structure of perovskite-type oxides. *Chem. Lett.* **13**, 893–896 (1984).
25. H.M. Zhang, Y. Shimizu, Y. Teraoka, N. Miura, and N. Yamazoe: Oxygen sorption and catalytic properties of $La_{1-x}Sr_xCo_{1-y}Fe_yO_3$ perovskite-type oxides. *J. Catal.* **121**, 432–440 (1990).
26. L. Xue, C. Zhang, H. He, and Y. Teraoka: Catalytic decomposition of N_2O over CeO_2 promoted Co_3O_4 spinel catalyst. *Appl. Catal., B* **75**, 167–174 (2007).
27. H. Vidal, J. Kašpar, M. Pijolat, G. Colonb, S. Bernal, A. Cordón, V. Perrichon, and F. Fally: Redox behavior of CeO_2–ZrO_2 mixed oxides: I. Influence of redox treatments on high surface area catalysts. *Appl. Catal., B* **27**, 49–63 (2000).
28. H.R. Aghabozorg, F. Sakhaie, M. Ramezani, and H. Aghabozorg: Doping of Sm into CeO_2 nanotubes up to 50%. *J. Sci. I. A. U. (JSIAU)* **19**, 47–52 (2009).
29. M. Yashima and T. Wakitak: Atomic displacement parameters and structural disorder of oxygen ions in the $Ce_xZr_{1-x}O_2$ solid solutions ($0.12 \leq x \leq 1.0$): Possible factors of high catalytic activity of ceria-zirconia catalysts. *Appl. Phys. Lett.* **94**, 171902 (2009).
30. M. Yashima, H. Arashi, M. Kakihana, and M. Yoshimura: Raman scattering study of cubic-tetragonal phase transition in $Zr_{1-x}Ce_xO_2$ solid solution. *J. Am. Ceram. Soc.* **77**, 1067–1071 (1994).
31. T. Nakatani, H. Okamoto, and R. Ota: Preparation of CeO_2-ZrO_2 mixed oxide powders by the coprecipitation method for the purification catalysts of automotive emission. *J. Sol-Gel Sci. Technol.* **26**, 859–863 (2003).
32. J. Kašpar, P. Fornasiero, and M. Graziani: Use of CeO_2-based oxides in the three-way catalysis. *Catal. Today* **50**, 285–298 (1999).
33. T. Masui, T. Ozaki, K. Machida, and G. Adachi: Preparation of ceria–zirconia sub-catalysts for automotive exhaust cleaning. *J. Alloys Compd.* **303–304**, 49–55 (2000).
34. G. Vlaic, R.D. Monte, P. Fornasiero, E. Fonda, J. Kašpar, and M. Graziani: Redox property–local structure relationships in the Rh-loaded CeO_2–ZrO_2 mixed oxides. *J. Catal.* **182**, 378–389 (1999).
35. J.L. Ayastuy, A. Gurbani, M.P. González-Marcos, and M.A. Gutiérrez-Ortiz: Selective CO oxidation in H_2 streams on $CuO/Ce_xZr_{1-x}O_2$ catalysts: Correlation between activity and low temperature reducibility. *Int. J. Hydrogen Energy* **37**, 1993–2006 (2012).
36. X. Wang, Q. Kang, and D. Li: Low-temperature catalytic combustion of chlorobenzene over MnO_x-CeO_2 mixed oxide catalysts. *Catal. Commun.* **9**, 2158–2162 (2008).
37. L. Cao, L. Pan, C. Ni, Z. Yuan, and S. Wang: Autothermal reforming of methane over $Rh/Ce_{0.5}Zr_{0.5}O_2$ catalyst: Effects of the crystal structure of the supports. *Fuel Process. Technol.* **91**, 306–312 (2010).
38. H. Zhang, Q. Yang, B. Zhang, and S. Lu: Raman spectroscopic investigation of lanthana-doped neodymium-yttria transparent ceramics. *J. Raman Spectrosc.* **42**, 1384–1387 (2011).
39. G.L. Markaryan, L.N. Ikryannikova, G.P. Muravieva, A.O. Turakulova, B.G. Kostyuk, E.V. Lunina, V.V. Lunin, E. Zhilinskaya, and A. Aboukaïs: Red-ox properties and phase composition of CeO_2-ZrO_2 and Y_2O_3-CeO_2-ZrO_2 solid solutions. *Colloids Surf., A* **151**, 435–447 (1999).
40. S.P. Kulyova, E.V. Lunina, V.V. Lunin, B.G. Kostyuk, G.P. Muravyova, and A.N. Kharlanov: Redox behavior of $Y_{0.05}Ce_{0.1}Zr_{0.85}O_2$ and $Y_{0.1}Ce_{0.1}Zr_{0.8}O_2$ system catalysts doped with copper(II). *Chem. Mater.* **13**, 1491–1496 (2001).
41. D. Terribile, A. Trovarelli, J. Llorcha, C. de Leitenburg, and G. Dolcctti: The synthesis and characterization of mesoporous high-surface area ceria prepared using a hybrid organic/inorganic route. *J. Catal.* **178**, 299–308 (1998).

https://doi.org/10.1557/jmr.2012.435 Published online by Cambridge University Press

42. E. Mamontov, T. Egami, A. Brezny, M. Koranne, and S. Tyagi: Lattice defects and oxygen storage capacity of nanocrystalline ceria and ceria-zirconia. *J. Phys. Chem. B* **104**, 11110–11116 (2000).
43. P. Fornasiero, T. Montini, M. Graziani, J. Kašpar, A.B. Hungria, A. Martinez-Arias, and J.C. Conesa: Effects of thermal pretreatment on the redox behaviour of $Ce_{0.5}Zr_{0.5}O_2$: Isotopic and spectroscopic studies. *Phys. Chem. Chem. Phys.* **4**, 149–159 (2002).
44. G. Balducci, P. Fornasiero, R. Di Monte, J. Kašpar, S. Meriani, and M. Grazini: An unusual promotion of the redox behaviour of CeO_2-ZrO_2 solid solutions upon sintering at high temperatures. *Catal. Lett.* **33**, 193–200 (1995).
45. L.F. Liotta, M. Ousmane, G. Di Carlo, G. Pantaleo, G. Deganello, G. Marcì, L. Retailleau, and A. Giroir-Fendler: Total oxidation of propene at low temperature over Co_3O_4–CeO_2 mixed oxides: Role of surface oxygen vacancies and bulk oxygen mobility in the catalytic activity. *Appl. Catal., A* **347**, 81–88 (2008).
46. C. Binet, M. Daturi, and J.C. Lavalley: IR study of polycrystalline ceria properties in oxidised and reduced states. *Catal. Today* **50**, 207–225 (1999).

https://doi.org/10.1557/jmr.2012.435 Published online by Cambridge University Press